nature astronomy

SUPPLEMENTARY INFORMATION

VOLUME: 1 | ARTICLE NUMBER: 0130

In the format provided by the authors and unedited.

Mass inventory of the giant-planet formation zone in a solar nebula analogue

Supplementary Table 1: Fixed model parameters for the disk of TW Hya

Stellar mass	Distance	Inner radius	Outer radius	inclination		Turbulence	Position angle
$M_\star$[8]	d[48]	r_{in}[49]	r_{out}	i[50]	V_{LSR}[51]	v_{turb}	PA[51]
($M_\odot$)	(pc)	(AU)	(AU)	(deg)	(km s^{-1})	(km s^{-1})	(deg)
0.6	55	2	150	7	2.8	0.01	155

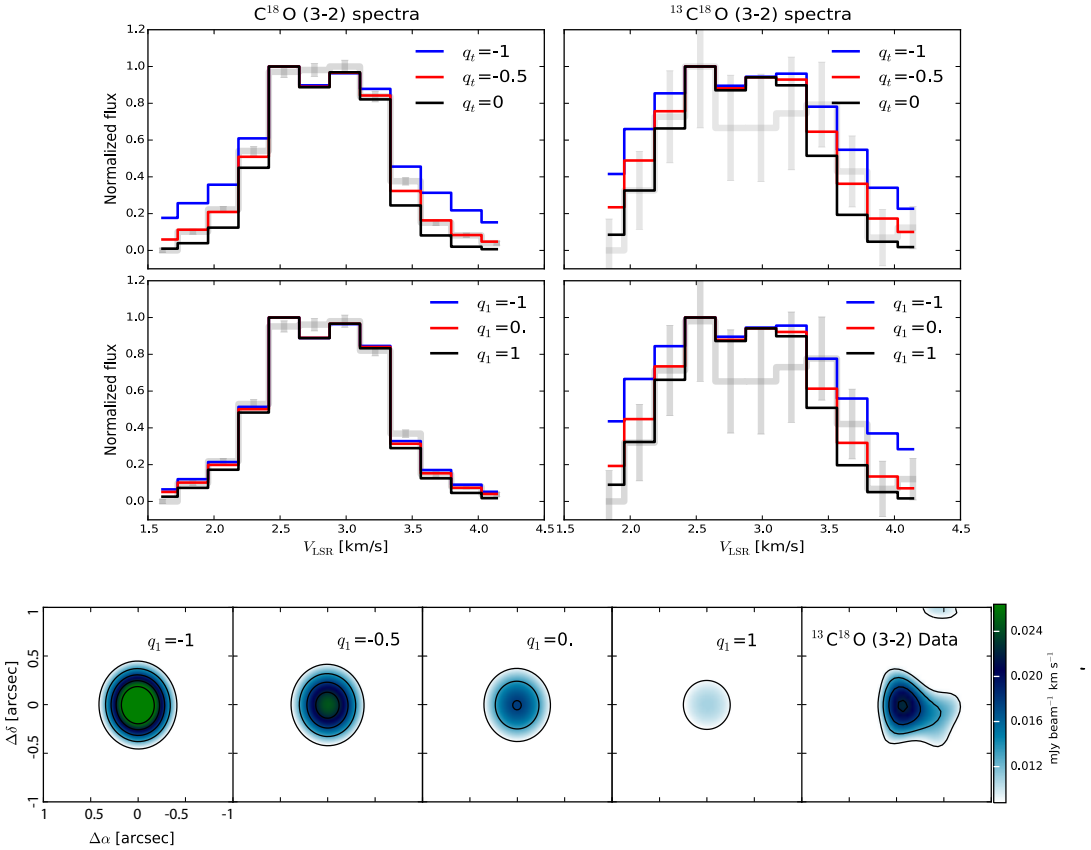

Supplementary Figure 1: Comparison of models with different temperature and optical depth distributions with the $^{13}C^{18}O$ and $C^{18}O$ (3-2) line spectra and $^{13}C^{18}O$ (3-2) moment zero map. All models adopt the best-fitting model parameters listed in Table 1 except for the q_t or q_1 values. The grey lines in the upper panel plots show line spectra and their uncertainty from the observations. In all plots, the flux at the central channel has been normalized to match with the best-fitting model. It can be seen that the spectral of the $C^{18}O$ is sensitive to temperature distribution (q_t) but not the optical depth distribution (q_1), and $^{13}C^{18}O$ (3-2) spectra and moment zero map is sensitive to both the temperature and optical depth distribution.

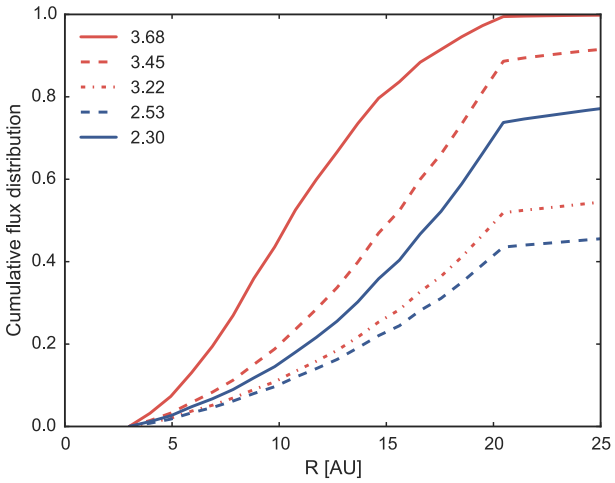

Supplementary Figure 2: Cumulative flux distributions of the $^{13}C^{18}O$ (3-2) line emission in the five velocity channels that have 3 σ detections, based on the best-fitting model. The LSR velocities of these channels are labelled at the upper left corner. Due to the regular Keplerian rotation velocity field in the disk, the radial dependence of flux contribution in a velocity channel varies from channel to channel. The figure shows that the 40-100% of the line emissions in these channels arise from regions inside the 21 AU, and indicates that each channel samples emissions at different radii with different weights. Therefore the radial distribution of the emission inside 21 AU can be constrained even the emission is only partially spatially resolved. The inner limit is $\sim$5 AU based on current observations (10% flux contribution in the 3.68 km s^{-1} channel).

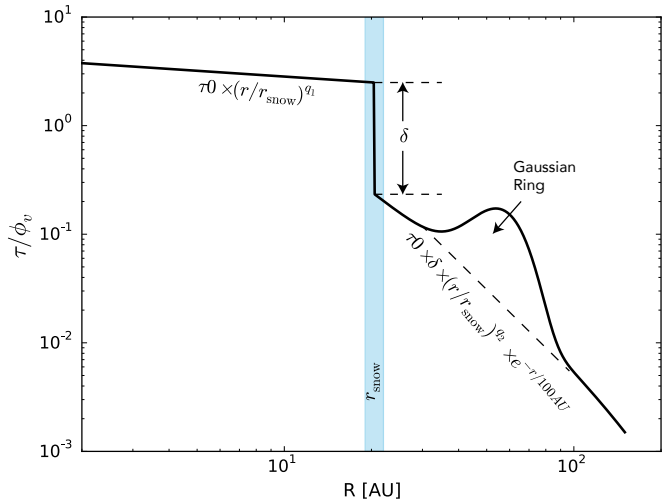

Supplementary Figure 3: The radial distribution of the integrated line strength of the parameterized model. The model structure consist of two distinct radial zones: inside and outside the mid-plane CO snowline. The two zones are used to model the break of the CO gas column density distribution due to condensation.

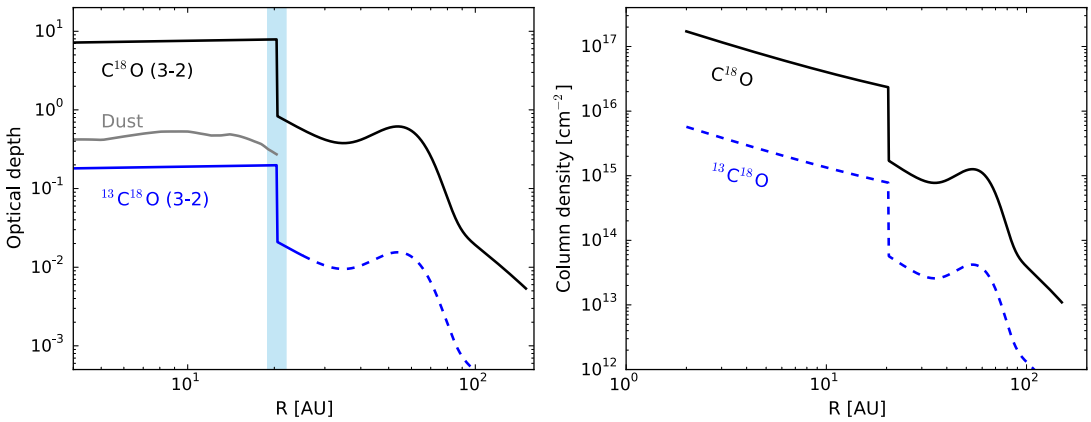

Supplementary Figure 4: Left: Optical depth at the center of the local line profile for the $C^{18}O$ (black) and $^{13}C^{18}O$ (blue) J=3-2 transitions, and for the 0.93 mm continuum emission. The optical depth of dust is only considered for the region within the CO snowline, because beyond that the CO line emission is mainly from a warm layer higher than the mid-plane. Right: Column density distribution of $C^{18}O$ and $^{13}C^{18}O$.

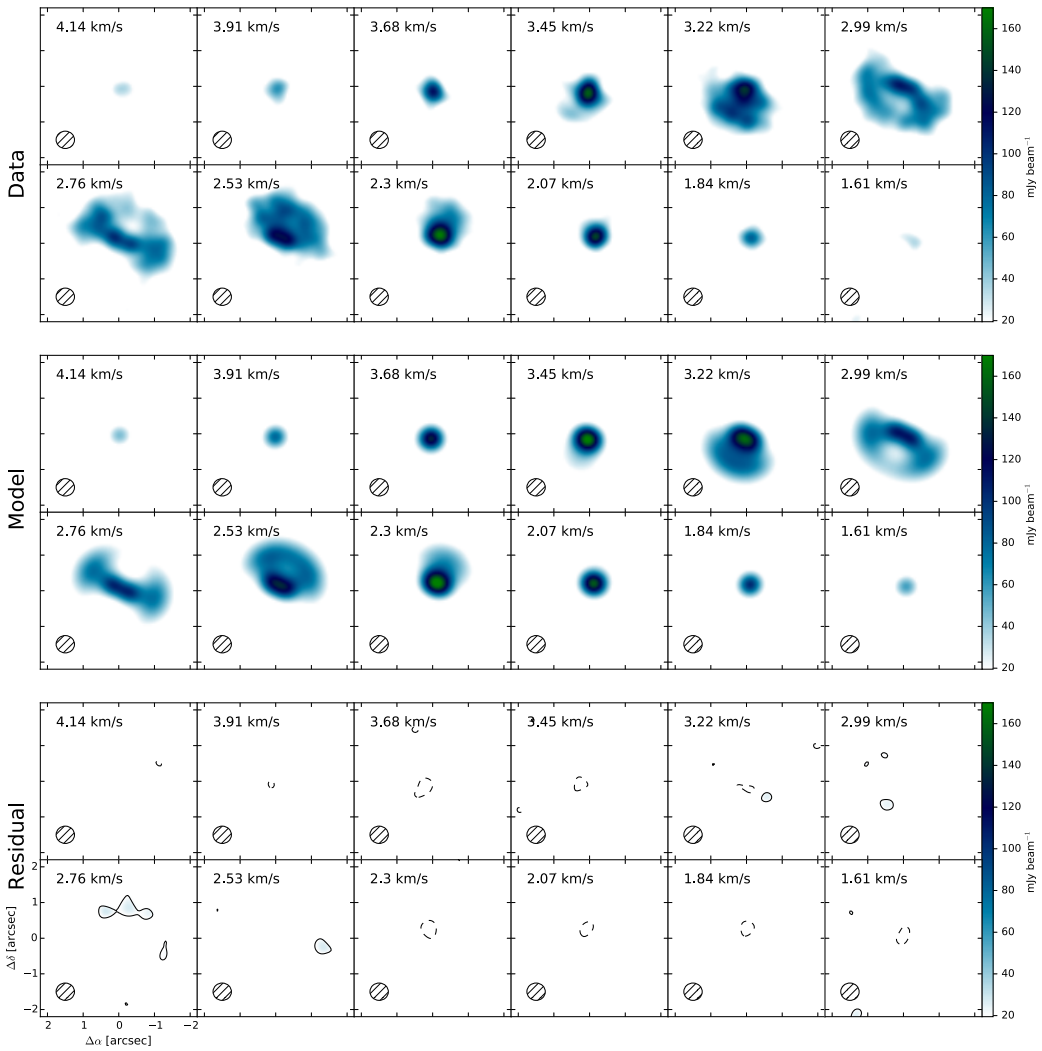

Supplementary Figure 5: Direct comparison of the observed $C^{18}O$ J=3-2 channel maps with synthetic data from the best-fit model in Table 1. The contour levels in the residual maps are set to be 3σ (solid line) and -3σ (dash line).

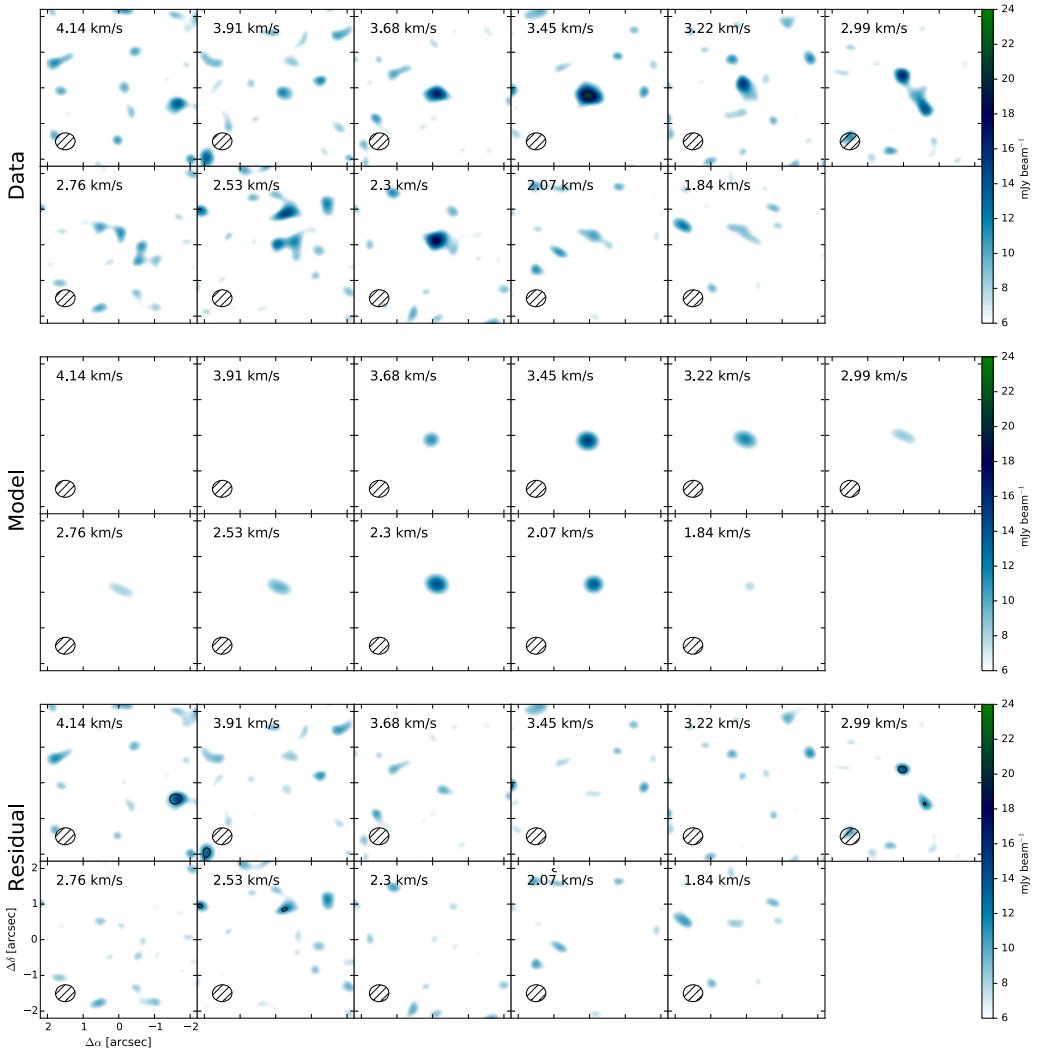

Supplementary Figure 6: Direct comparison of the observed $^{13}C^{18}O$ J=3-2 channel maps with synthetic data from the best-fit model in Table 1.

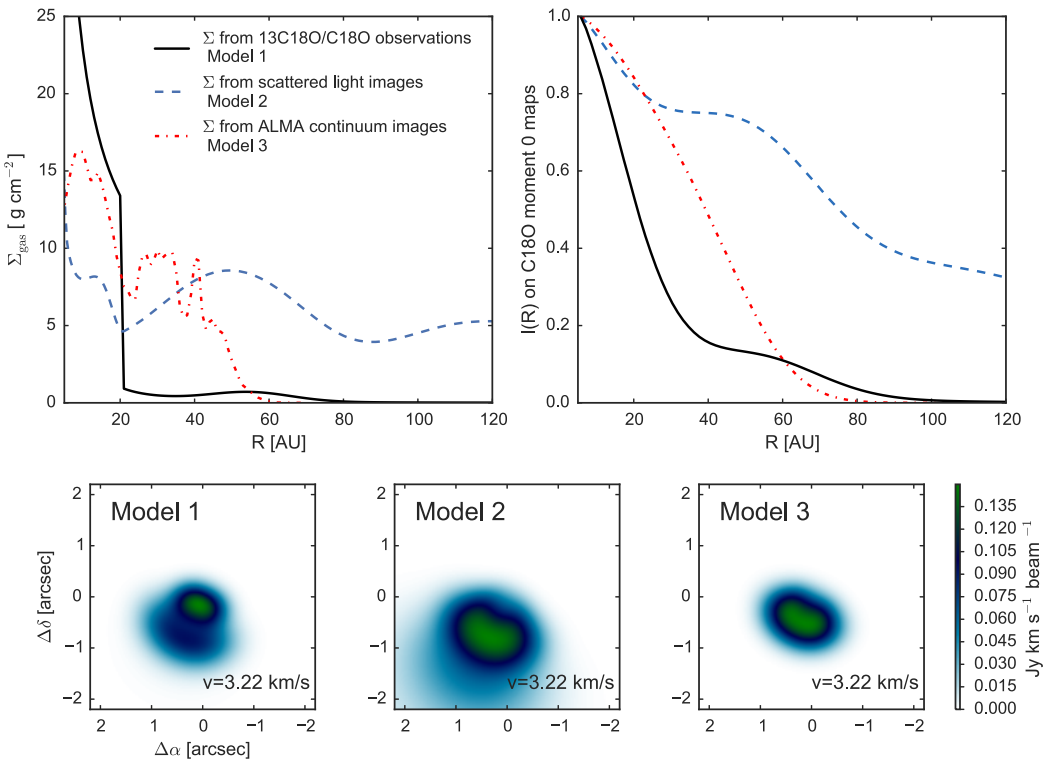

Supplementary Figure 7: The $C^{18}O$ (2-1) line emissions predicted by three models of the gas surface density distribution. Upper Left: The gas surface density profiles from three different models. Model 1 is the best-fitting model of this work, Model 2 is based on near Infrared scattered light images (ref. 42), and Model 3 is derived from the 345 GHz continuum emission. Upper Right: the radial profiles of the $C^{18}O$ (2-1) line moment zero map from the three models. It shows that the dust emission based models fail to reproduce the steep intensity decrease around 21 AU in the $C^{18}O$ observations. Lower panels: The $C^{18}O$ (2-1) line emission at the 3.22 km s^{-1} channel predicted by the three models. Only Model 1 can reproduce the narrow central peak observed in the $C^{18}O$ line emissions (see Supplementary Figure 5). The comparison of these models show that the sudden jump in the CO gas column density around 21 AU is not seen in either small or large dust particle distributions and it is most likely caused by CO sublimation at the mid-plane.

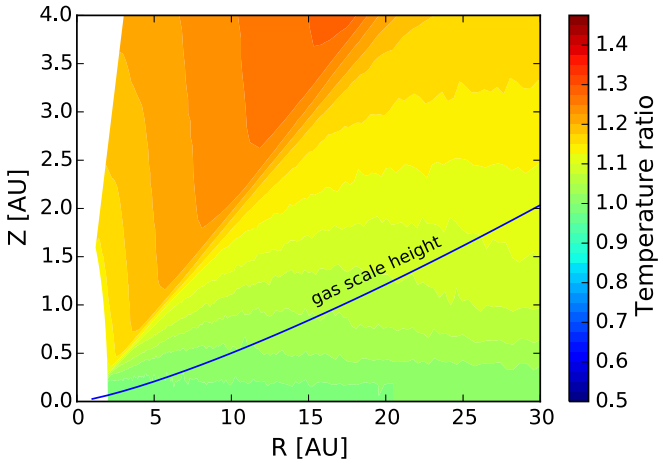

Supplementary Figure 8: Map of the temperature ratio between a small and a large dust grain populations for a representative radiative transfer model of the TW Hya disk. The vertical scale height of the large dust grain population is only 20% of that of the small dust population.

48. van Leeuwen, F. Validation of the new Hipparcos reduction. *Astron. & Astrophys.* **474**, 653–664 (2007).

49. Rosenfeld, K. A. *et al.* Kinematics of the CO Gas in the Inner Regions of the TW Hya Disk. *Astrophys. J.* **757**, 129 (15pp) (2012).

50. Qi, C. *et al.* Imaging the Disk around TW Hydrae with the Submillimeter Array. *Astrophys. J.* **616**, L11–L14 (2004).

51. Hughes, A. M., Wilner, D. J., Andrews, S. M., Qi, C. & Hogerheijde, M. R. Empirical Constraints on Turbulence in Protoplanetary Accretion Disks. *Astrophys. J.* **727**, 85 (17pp) (2011).